

Asymptotic behaviour of granular materials

David Mašín

Received: — / Accepted: —

Abstract The concept of the asymptotic behaviour of particulate materials is described, including its enhancement by considering asymptotic states in extension. A 3D discrete element model with elastic spherical particles and the granulometry of a real sand is set up. The numerical sample is stretched from different initial states, and the influence of the strain rate direction on the final state is studied within the stress ratio, void ratio and mean stress space. Asymptotic behaviour is clearly observed, although the grains remain intact (no grain crushing is considered). The extension asymptotic states are observed, and the notion of a normal extension line is introduced. The extension asymptotic states coincide with the peak states observed in the shear tests with constant stress path direction in dense samples.

Keywords asymptotic behaviour · critical state · discrete element method · particle crushing · sand

1 Introduction

Asymptotic behaviour is one of the most striking features in the behaviour of granular materials. Specific asymptotic states have been known since the early studies of soil mechanics. Casagrande [4], Hvorslev [27] and Taylor [60] are among the pioneers who observed critical state behaviour of soils – a particular asymptotic state related to constant volume shearing. Schofield and Wroth [54] and Roscoe and Burland [52] combined the existence of critical states and compression asymptotic

states (revealed in normal compression behaviour) into a unified framework of critical state soil mechanics. More generally, Gudehus et al. [24, 21] understood asymptotic states to be attractors in the behaviour of granular materials, which are independent of the initial state. They proposed that each direction of strain rate with a volume decrease is uniquely linked to a particular asymptotic stress ratio and a particular path in the mean stress vs. void ratio plane (normal compression line). Gudehus [22] later argued that the asymptotic stress ratio should not be expected to remain constant in the course of loading because of grain crushing and changing granulometry. The asymptotic state has also been denoted as the state limit [25], or the swept-out-memory state [24]. More recently, Gudehus [23] and Gudehus and Mašín [25] have extended the asymptotic state concept into the volume increase (extension) regime, and identified theoretical limits to the asymptotic behaviour. The "extension asymptotic states" have not yet been observed experimentally.

Asymptotic behaviour has been the subject of experimental investigation; critical state and normal compression behaviour have been well documented. More generally, compression asymptotic states have been studied, and confirmed, by Goldscheider [20] and Chu and Lo [9], who performed true and axisymmetric triaxial tests on sands with strain path control. They observed a unique relationship between the strain path direction and asymptotic stress ratio. Asymptotic behaviour has also been studied by testing fine-grained soils (clays), most notably by Topolnicki et al. [61]. They observed that the stress paths of tests starting at an arbitrary state became parallel to the asymptotic path in some cases. Further insight into the micro-mechanics of granular materials has been given, for example, in [19].

David Mašín
Charles University in Prague, Faculty of Science, Albertov 6,
12843 Prague 2, Czech Republic
Tel.: +420-2-21951552
Fax: +420-2-21951556
E-mail: masin@natur.cuni.cz

Another means of investigating the asymptotic state is the discrete element method (DEM). Different authors typically focused on specific asymptotic states; the existence of the critical state is confirmed in [56, 53, 65, 48, 7, 8, 67]. Salot et al. [53] and Wang et al. [65] demonstrated that the value of the critical state friction angle depends on the particle shape. The influence of the particle shape on the asymptotic behaviour was also emphasized in [30, 17, 33, 38, 57]. Luding and Alonso-Marroquín [36] observed that the critical state friction angle was constant for non-adhesive contact behaviour, but showed a pressure dependence for adhesive inter-particle contacts. For further details of the theoretical investigation of the micromechanics of granular assemblies, the reader is referred to [1, 51, 32] and the references therein.

A number of authors argued that the existence of asymptotic states is directly linked to particle crushing [64, 2, 7, 8, 44, 45, 43]. Using DEM simulations, the existence of normal compression lines was explained by particle crushing in references [64, 2, 7, 8, 44]. Cheng et al. [7, 8] predicted both critical states and normal compression lines, using the same parameter sets, creating a more complete picture of the granular material behaviour. They argued that particle crushing is a cause of the asymptotic behaviour.

The aim of this paper is to provide a detailed characterisation of the asymptotic behaviour of particulate materials. After introducing the asymptotic state framework, a comprehensive DEM model is set up. Using this model, numerical experiments were performed to reveal the asymptotic states. This included characteristics that have not been investigated before, such as the asymptotic behaviour in extension. It is also discussed whether particle crushing is a cause, or a consequence, of the asymptotic properties of granular assemblies.

2 Asymptotic state framework

Asymptotic state is defined as that state reached after a sufficiently long proportional stretching, i.e. stretching with a constant direction of the strain rate. Conceptual representation of asymptotic states has been proposed by Gudehus [23] and Gudehus and Mašín [25]. In this work, we focus on axisymmetric stress and deformation states, where the strain rate tensor is fully characterised by axial $\dot{\epsilon}_a$ and radial $\dot{\epsilon}_r$ components. Similarly, the stress tensor is given by σ_a (axial stress) and σ_r (radial stress). It is assumed that the granular material behaviour is governed only by its stress state and void ratio e (defined as the void volume over the solid volume). The strain rate direction may be characterised

by an angle ψ_ϵ (see Figure 1a), and the stress obliquity is quantified by the angle ψ_σ (Figure 1b).

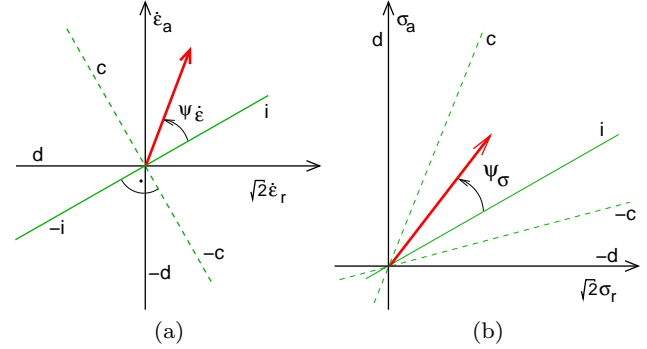


Fig. 1 Definition of angles ψ_ϵ and ψ_σ [25]. "i" denotes the isotropic direction, "c" denotes the isochoric (constant volume) direction, and "d" denotes the theoretical limit for asymptotic state behaviour.

2.1 Compression and constant volume asymptotic states

According to the current understanding of the asymptotic behaviour of a granular assembly, proportional deformation (constant ψ_ϵ) will ultimately lead to an asymptotic state characterised by a constant ψ_σ . Not all stretching directions will, however, lead to a unique asymptotic state. First, we focus on compression and constant volume stretching paths, characterised by a volume decrease (constant volume in the limiting case) and $-90^\circ \leq \psi_\epsilon \leq 90^\circ$. These directions of ψ_ϵ are represented in Figure 2a. Isotropic compression¹ $\psi_\epsilon = 0^\circ$ is indicated with the index 'i'; limiting values $\psi_\epsilon = \pm 90^\circ$ (constant volume shearing) with the index 'c'. Each ψ_ϵ is related to a unique asymptotic value of ψ_σ , as demonstrated in Figure 2b. In the special case of isochoric deformation ($\pm c$, critical state), the corresponding value of ψ_σ is directly linked to the critical state friction angle by

$$\tan \psi_{\sigma(\pm c)} = \pm \left(\frac{2\sqrt{2} \sin \varphi_c}{3 \mp \sin \varphi_c} \right) = \frac{\sqrt{2}}{3} M \quad (1)$$

where $M = q/p$ at the critical state ($p = (\sigma_a + 2\sigma_r)/3$, $q = \sigma_a - \sigma_r$). Each of the asymptotic states also have a unique trace in the mean stress p vs. void ratio e plane (Figure 2c). Asymptotic states in this plane are traditionally denoted as normal compression lines. In some soils (mainly clays), they are found to be linear in

¹ Note that the isotropic asymptotic state is defined here by $\psi_\epsilon = 0^\circ$; the corresponding asymptotic ψ_σ may then differ from 0° in the case of anisotropic structure.

the $\ln p$ vs. $\ln(1+e)$ plane [3], but this is not a general rule. All normal compression lines are bound between isotropic normal compression line, attributed to $\psi_{\dot{\epsilon}(i)}$, and the critical state line, linked with $\psi_{\dot{\epsilon}(\pm c)}$. Different measures have been defined throughout the literature to represent the position of the given normal compression line. The two most commonly used are the relative void ratio r_e and the overconsolidation ratio OCR^2

$$r_e = \frac{e - e_d}{e_c - e_d} \quad OCR = \frac{p_e^*}{p} \quad (2)$$

where e_d and e_c are minimum and critical state void ratios at the current mean stress respectively. p_e^* is the Hvorslev equivalent pressure, defined as the mean stress at the isotropic normal compression line at the current void ratio. It is clear that the isotropic normal compression line is characterised by $r_e = r_{ei} > 1$ and $OCR = 1$, and the critical state line by $r_e = 1$ and $OCR = OCR_c > 1$. Each of the compression asymptotic states can be attributed to a unique value of $1 \leq r_e \leq r_{ei}$, or $OCR_c \geq OCR \geq 1$.

Compression asymptotic states are predicted by constitutive models based on the critical state theory, such as the Modified Cam clay model [52], or hypoplastic models [66,39,40]. The models incorporate the notion of a state boundary surface (SBS), which is defined as a boundary of all possible states in the stress vs. void ratio space. For the purpose of the present discussion, we also define the asymptotic state boundary surface (ASBS) (also known as the swept-out-memory surface [41]), which is an envelope of all asymptotic states. Critical state soil mechanics models consider the two surfaces to coincide. A constant void ratio cross-section through this surface in the compression regime is sketched in Figure 2d. In the principal stress vs. void ratio space, the ASBS is a four-dimensional object; this is shown in Figure 3d for the axisymmetric case.

An important property of compression asymptotic states is that they may be reached by proportional compression from the stress-free state.

2.2 Extension asymptotic states

Asymptotic behaviour in compression and under constant volume is considered to be a well-proven property of a granular assembly. However, the contrary is true regarding asymptotic behaviour in extension. As suggested by Gudehus [23] (Chapters 2 and 3) and Gudehus and Mašín [25], asymptotic states can also

² OCR is traditionally defined as $OCR = p_c/p$, where p_c is the preconsolidation pressure. We prefer the definition (2), as no additional assumptions about the quasi-elastic soil behaviour are needed for its quantification.

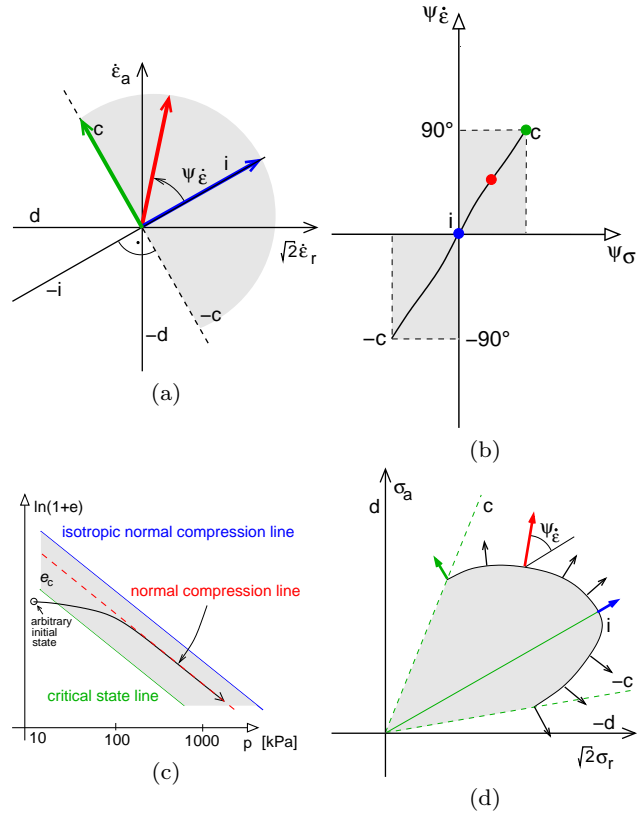


Fig. 2 Graphical representation of compression asymptotic states. Zones relevant to asymptotic states in compression are highlighted in grey.

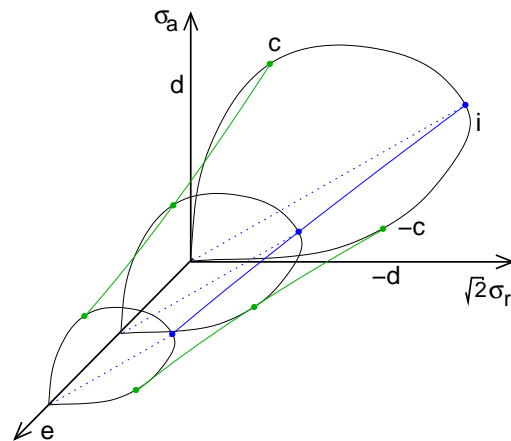


Fig. 3 Sketch of the asymptotic state boundary surface in the stress vs. void ratio space for the axisymmetric case.

be reached after proportional stretching along extension (volume increase) paths. These asymptotic states have, to the author's knowledge, not yet been observed experimentally; their existence is expected solely from theoretical arguments. The stretching directions that lead to extension asymptotic states are depicted in Figure 4a. Limiting values of $\psi_{\dot{\epsilon}}$ and ψ_{σ} are denoted with indices 'd' (asymptotic $\sigma_r = 0$) and '-d' (asymptotic

$\sigma_a = 0$) [25]. The maximum values of $|\psi_\sigma|$ at the limiting states $\pm d$ correspond to mobilised friction angles equal to 90° . The relationship between $\psi_\dot{\epsilon}$ and ψ_σ for asymptotic extension paths is shown in Figure 4b.

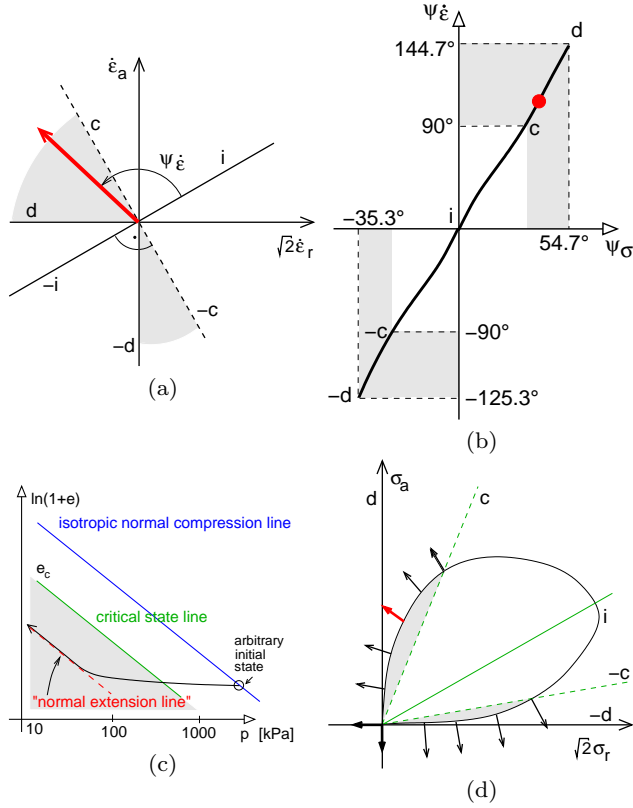


Fig. 4 Graphical representation of extension asymptotic states. Zones relevant to asymptotic states in extension are highlighted in grey.

Each extension asymptotic state is also associated with its trace in the mean stress vs. void ratio plane. In the following, we denote these traces as *normal extension lines* (adopting a parallel with the well-known notion of normal compression lines), seen in Figure 4c. Gudehus [23] suggested that the minimum void ratio e_d represents a normal extension line for states $\pm d$. Because proportional stretching along extension asymptotic states involves volume increase and mean stress decrease, these states cannot be approached from the stress-free state.

Interestingly, although knowledge of the extension asymptotic states is scarce, these states are predicted by virtually all constitutive models based on critical state soil mechanics (for example, [52,66,39,37]). The reason for this may be explained with the aid of Figure 4d, which shows a complete ASBS of a granular material, with the highlighted portion corresponding to the extension asymptotic states. The models were de-

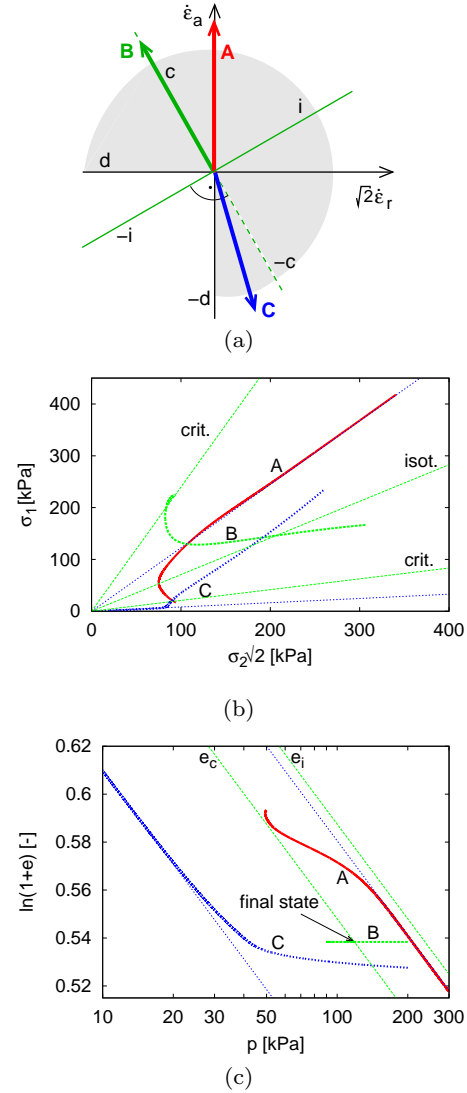


Fig. 5 Asymptotic properties of the hypoplastic model developed by Mašín [39]. The simulations are from [25].

veloped to correctly represent the so-called *peak states*. Peak states are attained after loading with the stress paths in a fixed direction (for example, a drained triaxial test, which is characterised by $\dot{\sigma}_r = 0$). It has been shown experimentally that such loading, from the initial state with $r_e < 1$ ($OCR > OCR_c$), leads to a higher mobilised friction angle than that which corresponds to $\pm c$ states. The strain rate at the peak state is dilatant. To represent this behaviour, the SBS for $r_e < 1$ extends into the region of $|\psi_\sigma| > |\psi_{\sigma(\pm c)}|$, with $|\psi_\dot{\epsilon}| > |\psi_{\dot{\epsilon}(\pm c)}|$, as depicted in Figure 4d.

As mentioned earlier, ASBS in the critical state models is considered to coincide with the SBS. For this reason, constitutive models based on critical state soil mechanics implicitly predict extension asymptotic states,

although the model developers did not specifically aim to predict them.

To demonstrate the asymptotic property of constitutive models, Figure 5 shows the predicted compression (path "A"), constant volume (path "B") and extension (path "C") asymptotic state using the critical state soil mechanics-based hypoplastic constitutive model of Mašin [39]. This model is capable of predicting all three types of asymptotic states; the explicit mathematical formulation of the asymptotic states predicted by this model are given in [41].

3 Discrete element model characteristics

In order to model the granular assembly, the open-source 3D discrete element software Yade [63] was used. This software utilises the DEM formulation by Cundall and Strack [13]. The algorithm involves two steps: First, based on constitutive laws, the interaction forces between the discrete elements are computed. The elements are allowed to slightly interpenetrate each other, which actually represents the relative deformation of the surface layers of the particles [12]. Second, Newton's second law is applied to determine, for each element, the resulting acceleration, which is then time integrated to find its new position. This process is repeated until the simulation is finished [55, 15]. Chen et al. [6] demonstrated that the Yade software yields comparable predictions to the commercial software package PFC [28].

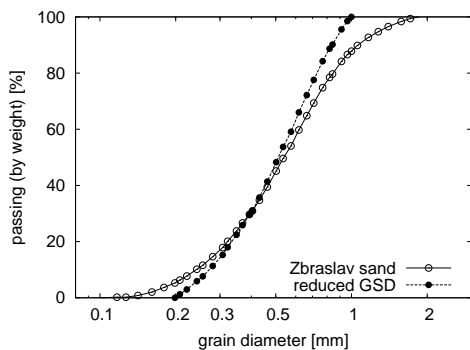


Fig. 6 Grain size distribution of Zbraslav sand from [16], and the reduced grain size distribution adopted in the simulations.

We present the results for a specimen consisting of elastic spherical particles. To eliminate the influence of the model boundaries, periodic boundary conditions have been adopted [46], so that the modelled unit cell (as well as all its particles and all their properties) is surrounded by identical cells shifted along the cell edges

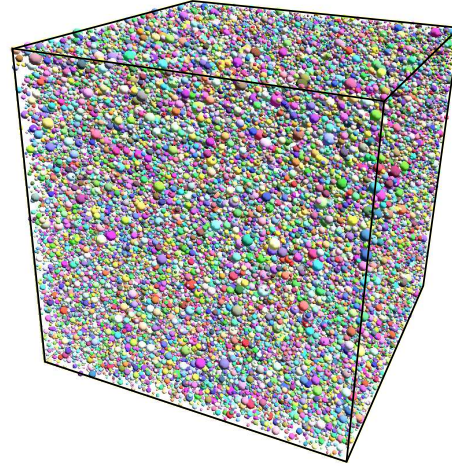


Fig. 7 Periodic cell used in the simulations, consisting of 150000 spherical particles.

[58]. In order to resemble a real granular material, particles of different sizes have been considered following the grain-size-distribution curve of a real sand. Figure 6 shows grain size distribution of Zbraslav sand [16]. For the purpose of the discrete element modelling, particles above 1 mm and below 0.2 mm were removed from the specimen ("reduced GSD" in Figure 6). The sample consisted of 150000 spherical particles, generated using an algorithm to ensure that they followed the prescribed particle size distribution, were randomly distributed, and were initially not in contact. The periodic cell was cubic, with the initial side length of 31 mm. The specimen was generated only once and used in all subsequent simulations; all the results thus represent the response of an identical sample. It has been verified that practically identical results were obtained if new sample was generated in each simulation. The specimen in its initial state is depicted in Figure 7.

The contact properties of the spherical particles were governed by a basic linear elastic perfectly plastic model without cohesion [13], which specifies the contact normal stiffness k_n , shear stiffness k_s and friction angle φ . These parameters are calculated from the particle properties E (Young's modulus), ν (Poisson's ratio) and φ . In the present simulations, constant values $E = 500$ MPa, $\nu = 0.3$ and $\varphi = 0.5$ Rad (coefficient of friction $\mu = 0.546$) have been used. The rolling resistance (rotational spring) was not considered. The prescribed particle density was $\rho_s = 2650$ kg/m³ and acceleration due to gravity was zero. The influence of selected contact parameter values is clarified in Sec. 5.

The periodic cell boundaries were subjected to a constant velocity gradient ∇v , which means to constant value of the Euler stretching tensor $\mathbf{D} = (\partial v_i / \partial x_j +$

$\partial v_j / \partial x_i) / 2$, as no rotations have been considered. Axisymmetric conditions were applied, such that $D_{22} = D_{33}$ (subscripts 2 and 3 represent the horizontal directions, 1 the vertical direction). The angle ψ_ε can then be calculated by means of Figure 1a, where $\dot{\varepsilon}_a = D_{11}$ and $\dot{\varepsilon}_r = D_{22} = D_{33}$. Off-diagonal components of \mathbf{D} are always zero. A constant magnitude of the stretching rate $\|\mathbf{D}\| = \sqrt{\mathbf{D} : \mathbf{D}} = 167 s^{-1}$ and step size $\Delta t = 1.2 * 10^{-7} s$ was applied at all times. Local non-viscous damping [11, 5], has been used, with a damping coefficient $\chi = 0.5$. The influence of the selected step size and stretching rate is discussed in more detail in Sec. 5.

The simulation results have been evaluated in terms of the Cauchy stress tensor $\boldsymbol{\sigma}$ and void ratio e . The void ratio has been calculated from the current cell size and total particle volume (particle overlaps have thus been neglected). The macroscopic stress $\boldsymbol{\sigma}$ was obtained from the inter-particle forces using the procedure outlined in [31]. The angle ψ_σ was calculated using Figure 1b, with $\sigma_a = \sigma_{11}$ and $\sigma_r = (\sigma_{22} + \sigma_{33}) / 2$ (note that the slight difference between σ_{22} and σ_{33} has occurred due to the initial random inhomogeneities of the sample). Only positive values of the angle ψ_ε were considered in this study.

An increase in the magnitude of particle overlaps decreases the accuracy and the physical relevance of the simulations; this overlap magnitude is quantified in Figure 8, where the distribution of the relative overlap magnitude is plotted for several stress levels along the $\psi_\varepsilon = 0^\circ$ asymptotic stress path. At around a stress of 1MPa, the maximum relative overlap magnitude reaches 2%. The stress of 1MPa is considered to be an approximate limit of accuracy for the present simulations. At 10 MPa the relative overlaps reach 10%, which renders the results unreliable. At stresses lower than 100 kPa the relative overlaps are small, lower than 0.5%. Figure 8 also demonstrates that an increase in the stress level is associated with a dramatic increase in the number of inter-particle contacts.

4 DEM simulation results

4.1 Compression and constant volume asymptotic states

First, we investigate the compression and constant volume asymptotic states. Figure 9 shows results on a sample loaded uniformly along the path $\psi_\varepsilon = 0^\circ$, together with the results of a test where the loading direction was reversed several times to $\psi_\varepsilon = 180^\circ$. The uniformly loaded sample clearly defines an isotropic normal compression line, which is approximately linear in the $\ln p$

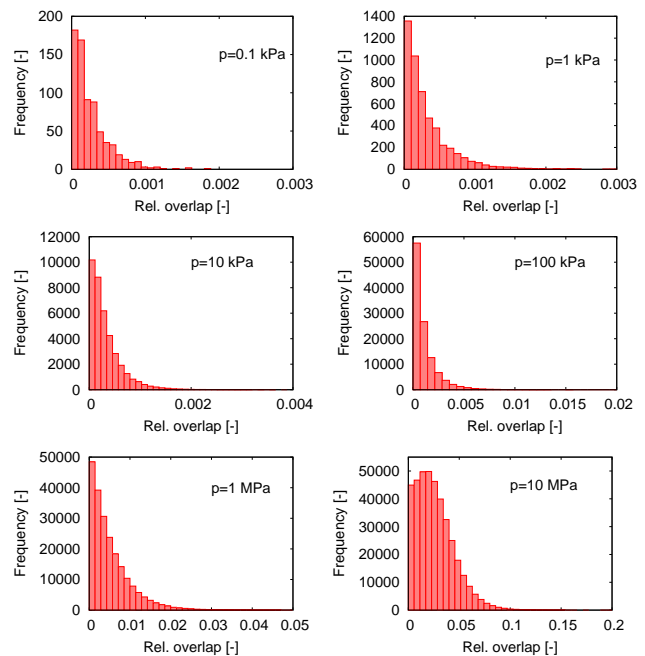


Fig. 8 Frequency – magnitude diagrams of relative overlaps $\Delta u / (r_1 + r_2)$ between particles in $\psi_\varepsilon = 0^\circ$ test. Δu is the overlap and r_1 and r_2 are radii of the spheres in contact.

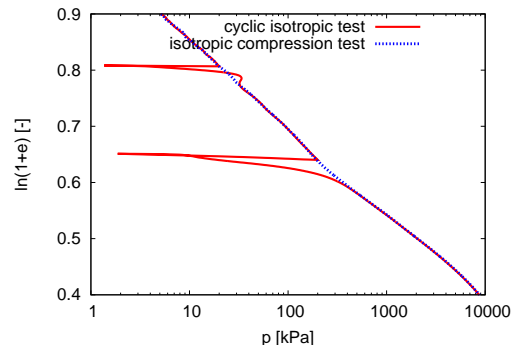


Fig. 9 Monotonous and cyclic (unloading-reloading) isotropic test results ($\psi_\varepsilon = 0^\circ$ in loading and $\psi_\varepsilon = 180^\circ$ in unloading).

vs. $\ln(1 + e)$ plane. The sample with the unloading-reloading cycles shows that the isotropic normal compression line is asymptotically approached irrespective of the initial soil density (apart from the minor "overshooting" in the first reloading cycle, which may be attributed to inertia effects). The normal compression behaviour was observed on an assembly of elastic (non-crushable) spheres; it is thus not related to grain crushing. Instead, grain crushing may be regarded as an eventual consequence of stress concentration during loading along the normal compression line.

Secondly, we study the constant volume asymptotic state ($\psi_\varepsilon = 90^\circ$). Figure 10 shows the results of constant volume experiments on normally consolidated samples.

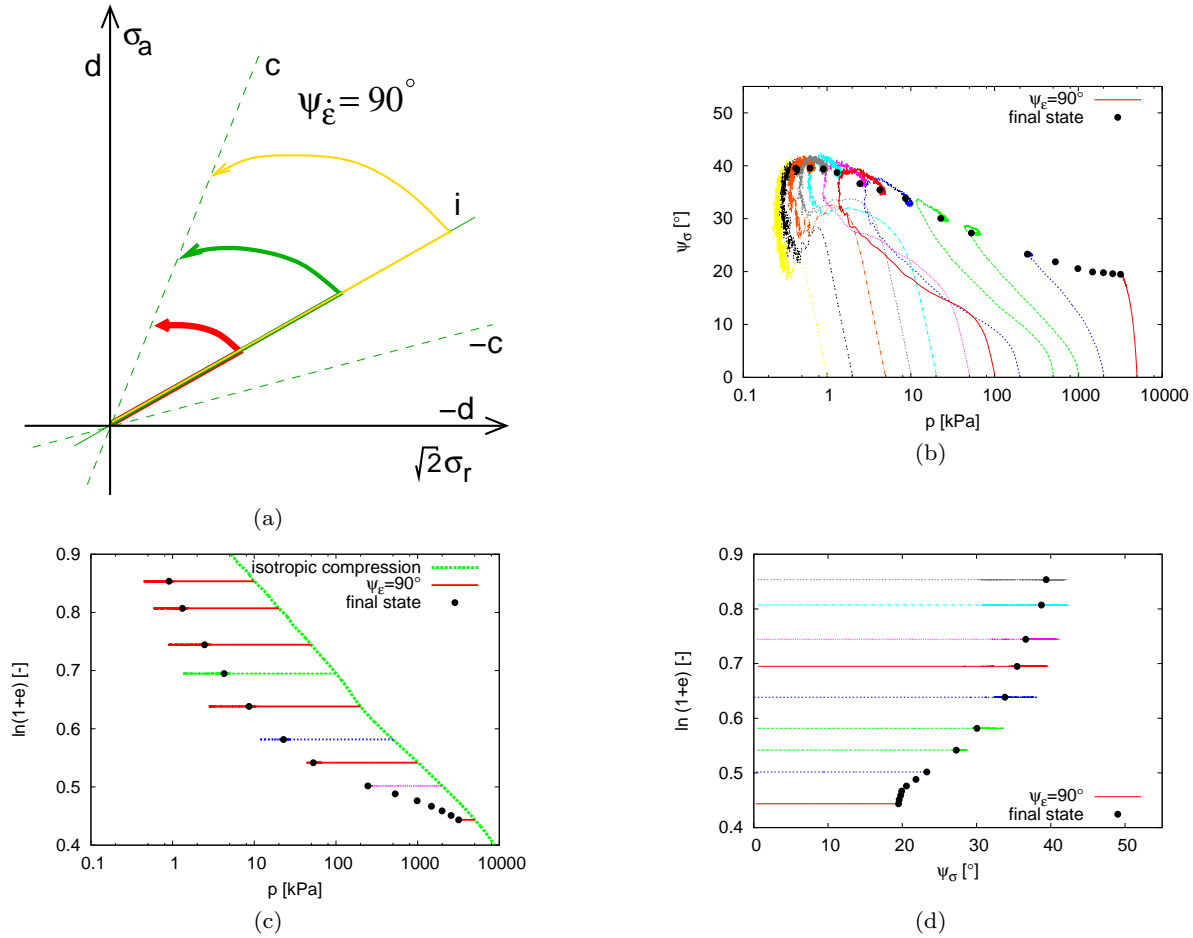


Fig. 10 $\psi_\varepsilon = 90^\circ$ tests on normally consolidated samples. (a) sketch of the stress paths expected from the theory, (b,c,d) results of DEM simulations. (b) ψ_σ vs. mean stress diagram, (c) normal compression lines in the $\ln(1+e)$ vs. $\log p$ plane, (d) ψ_σ vs. $\ln(1+e)$ diagram.

The samples were first loaded along the $\psi_\varepsilon = 0^\circ$ path up to the prescribed value of the mean stress. Then, the direction of loading was changed to $\psi_\varepsilon = 90^\circ$ and the samples were sheared until the asymptotic state was reached. The same procedure (with variable ψ_ε) was adopted in all subsequent simulations on normally consolidated (NC) samples. Figure 10a gives a sketch of the stress path followed, Figure 10b shows the p vs. ψ_σ path, Figure 10c the $\ln(1+e)$ vs. $\ln p$ response and Figure 10c the ψ_σ vs. $\ln(1+e)$ diagram. The final states appear to align along a single curve in the p vs. ψ_σ plane, but this curve is not represented by a constant value of ψ_σ . This is discussed in more detail in Sec. 5. The final states in the $\ln(1+e)$ vs. $\ln p$ plane form a clearly defined critical state line. This line is approximately parallel to the isotropic normal compression line, apart from the larger stresses, where the results are influenced by the final compressibility of the grains and consequent non-negligible overlapping of particles (see Figure 8).

Another set of numerical experiments was devised (Figure 11) to investigate the independence of the isochoric asymptotic state on the initial conditions. The samples were first loaded along the $\psi_\varepsilon = 0^\circ$ path until $p = 1000$ kPa, then unloaded along the $\psi_\varepsilon = 180^\circ$ path until different prescribed mean stresses were reached, and finally sheared along $\psi_\varepsilon = 90^\circ$ path up to the asymptotic state. The same procedure was adopted in all subsequent simulations on overconsolidated (OC) samples. All the samples thus had a similar initial void ratio (the differences were only caused by the relatively high unloading modulus of the assembly), but different relative void ratios r_e (different overconsolidation ratios OCR). For comparison, Figure 11 also shows the results on normally consolidated samples. The asymptotic states coincide exactly with the states reached after normal compression, demonstrating that the isochoric asymptotic state is independent of the initial stresses and void ratios. It is also interesting to point out that the maximum value of ψ_σ reached in the tests increases

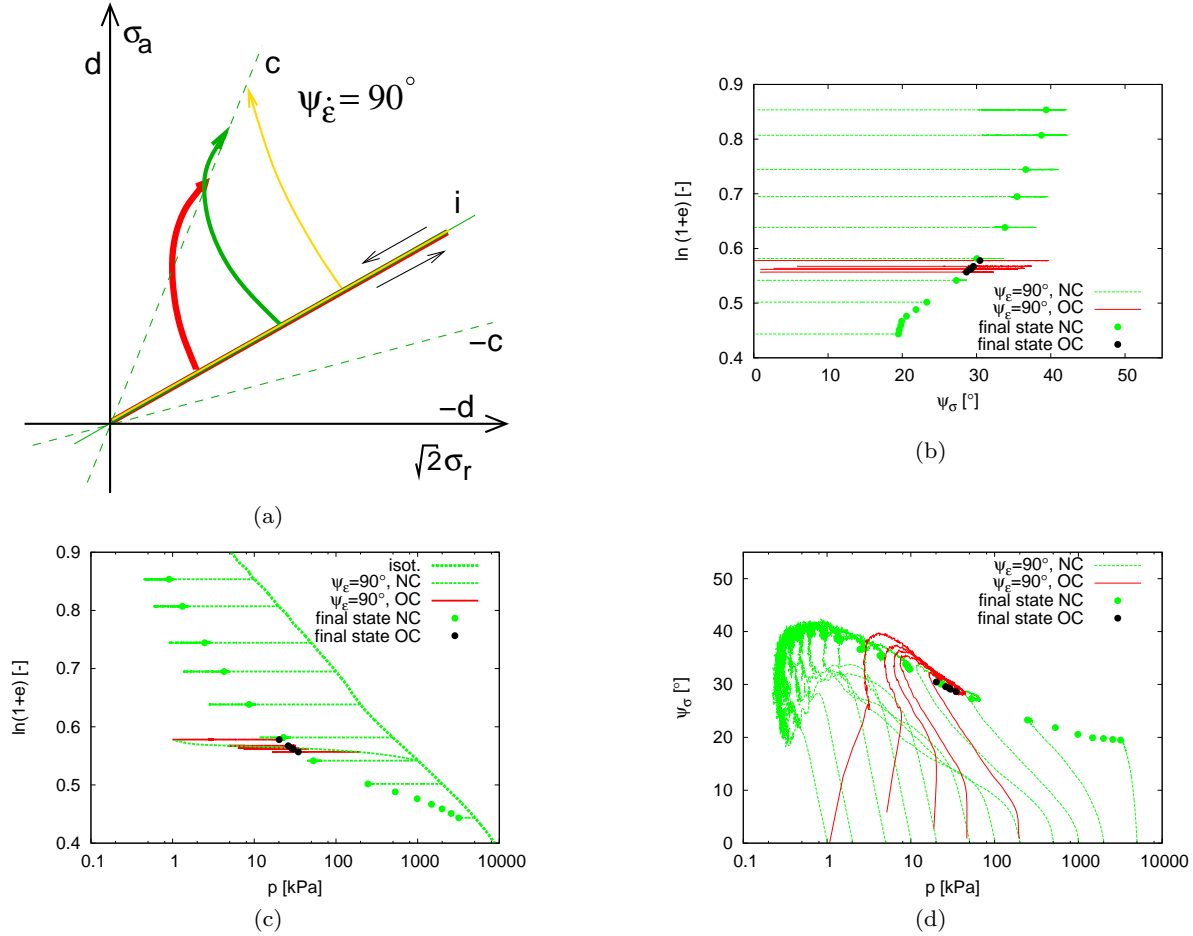


Fig. 11 $\psi_{\dot{\epsilon}} = 90^\circ$ tests on overconsolidated samples. (a) sketch of the stress paths expected from the theory, (b,c,d) results of DEM simulations. (b) ψ_σ vs. mean stress diagram, (c) normal compression lines in the $\ln(1+e)$ vs. $\log p$ plane, (d) ψ_σ vs. $\ln(1+e)$ diagram.

with increasing overconsolidation ratio. In other words, the peak friction angle increases with OCR , while the critical state friction angle remains unchanged. This is consistent with predictions using constitutive models based on critical state soil mechanics.

In the next set of simulations, we consider a shear test in which the stress path (rather than the strain path) direction is controlled. Namely, experiments with a constant σ_r (denoted as drained triaxial tests in soil mechanics terminology) have been simulated. The same stretching rate D_{11} as in the $\psi_{\dot{\epsilon}} = 90^\circ$ tests was imposed, and $D_{22} = D_{33}$ were controlled in such a way that σ_r remained constant. After sufficiently long shearing, the specimens reached a state with constant σ and constant e , therefore with constant ψ_σ and with $\psi_{\dot{\epsilon}} = 90^\circ$ (see Figure 12). Tests on both normally consolidated and overconsolidated samples were considered. The asymptotic states reached by the NC and OC samples coincided for the given σ_r (Figure 12). They, however, depended on the radial stress. The results are

compared with results of $\psi_{\dot{\epsilon}} = 90^\circ$ in Figure 13. The final states are close to the results of the tests with the $\psi_{\dot{\epsilon}} = 90^\circ$ strain path, but a slight deviation was observed. Note that the stress path at low stress obliquities deviated from the ideal constant σ_r path, caused by an imperfection in the σ_r control in the software. In the larger strain range and at asymptotic states, however, the results were not affected.

The next series of numerical experiments involves loading along compression proportional paths with $0^\circ < \psi_{\dot{\epsilon}} < 90^\circ$ (Figure 14). The test results for the given direction $\psi_{\dot{\epsilon}}$ converge towards a unique asymptotic state. Similarly to the isochoric asymptotic state, ψ_σ is not a constant depending primarily on $\psi_{\dot{\epsilon}}$, but in addition it depends on the current mean stress level. In agreement with the framework from Section 2, increasing $\psi_{\dot{\epsilon}}$ leads to a continuous increase of asymptotic ψ_σ (for a given mean stress). In the volumetric space (Figure 14c), increasing $\psi_{\dot{\epsilon}}$ leads to a continuous increase of the

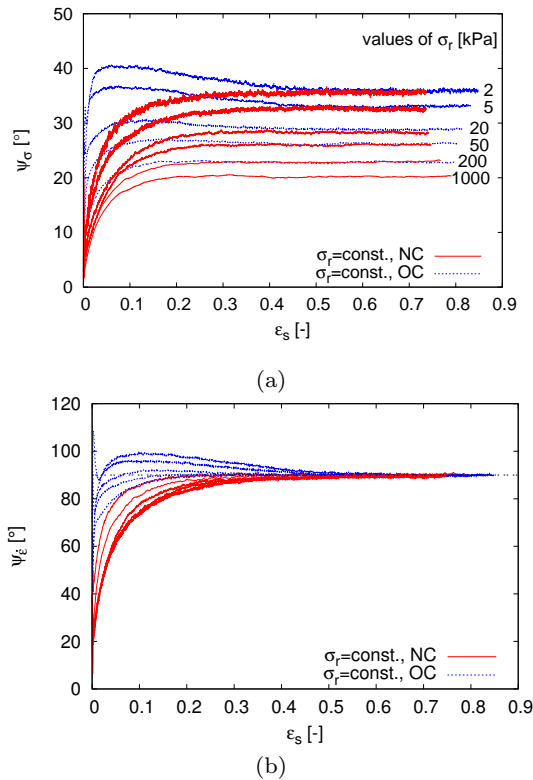


Fig. 12 Constant σ_r tests on normally consolidated and overconsolidated samples. (a) ψ_σ vs. $\epsilon_s = 2(\epsilon_a - \epsilon_r)/3$ graph, (b) ψ_ϵ vs. ϵ_s graph.

asymptotic *OCR*. The asymptotic value of *OCR* for the given ψ_ϵ depends on the void ratio e .

4.2 Extension asymptotic states

To track the extension asymptotic states, the same procedure adopted in the case of compression states is used with $\psi_\epsilon > 90^\circ$. The results are shown in Figure 15. The curves in Figure 15c form clearly defined normal extension lines; an increase in ψ_ϵ yields an increase in the *OCR* (for a given e), consistent with the framework outlined in Section 2. The asymptotic ψ_σ for the given void ratio e increases with ψ_ϵ for lower void ratios only. At higher void ratios, the asymptotic ψ_σ appears to be independent of ψ_ϵ in the $\psi_\epsilon > 90^\circ$ range. The maximum angle of ψ_ϵ , for which the asymptotic states could reasonably be studied, was $\psi_\epsilon = 110^\circ$. For higher angles, asymptotic state would have been reached at extremely low stresses (below 0.5 kPa), where the results were scattered and unreliable. We thus could not confirm the existence of the limit state denoted as $\pm d$ in Figure 4a.

4.3 Summary of the simulation results

Figure 16 attempts to summarise the asymptotic states obtained in the described discrete element simulations. While plotting Figure 16 it was necessary to decide whether the asymptotic state had already been reached. This has been done in an ad-hoc way. Experiments with ψ_ϵ close to 90° do not show any significant void ratio change during shearing; the final states reached in the experiments were thus considered to represent the asymptotic states. The relevance of this assumption is clear from Figure 12; the tests with $\psi_\epsilon < 80^\circ$ and $\psi_\epsilon > 100^\circ$ show a significant change in the void ratio and mean stress during compression (respective extension) along the asymptotic states. The final states reached in these experiments are thus insufficient to track the overall dependency of the asymptotic stress ratio on the mean stress (on void ratio). In these cases, portions of the test paths from Figs. 14 and Figs. 15, which were reached by a number of tests with different consolidation stresses, were plotted in Figure 16. Since the same state was reached by different tests, these states are considered to properly represent the asymptotic response.

Results from Figure 16 allowed us to plot the shapes of the ASBS cross-sections for constant void ratio, which are shown in Figure 17 in the plane of q vs. p normalised by the Hvorslev stress p_e^* . Our results imply that the shape of the constant void ratio cross-section through the ASBS depends on the value of the void ratio. The shape of the surface is close to the shape predicted by the hypoplastic models [39]. However, in the constitutive models, critical state conditions ($\psi_\epsilon = 90^\circ$) are typically located in the surface apex; in the present numerical experiments, they are located far to the left of it.

Figure 18 shows the normalised asymptotic state boundary surface at the void ratio $\ln(1+e) = 0.58$, plotted together with results of constant volume ($\psi_\epsilon = 90^\circ$) tests at different overconsolidation ratios. Namely, the results of normally consolidated test to $p = 500$ kPa and overconsolidated test unloaded to 1 kPa are plotted. Specimens in these two experiments had $\ln(1+e)$ very close to 0.58 (see Figure 11c). Figure 18a shows that both the stress paths are bound by the ASBS, indicating that the ASBS may well be considered as an approximation of the state boundary surface. Figure 18b, however, demonstrates that the $\psi_\epsilon = 90^\circ$ path does not follow the ASBS in the course of loading. This is consistent with predictions of hypoplasticity [39, 41, 42], but not with predictions of elasto-plastic models based on critical state soil mechanics [52]. The elasto-plastic models imply that in normally consolidated conditions

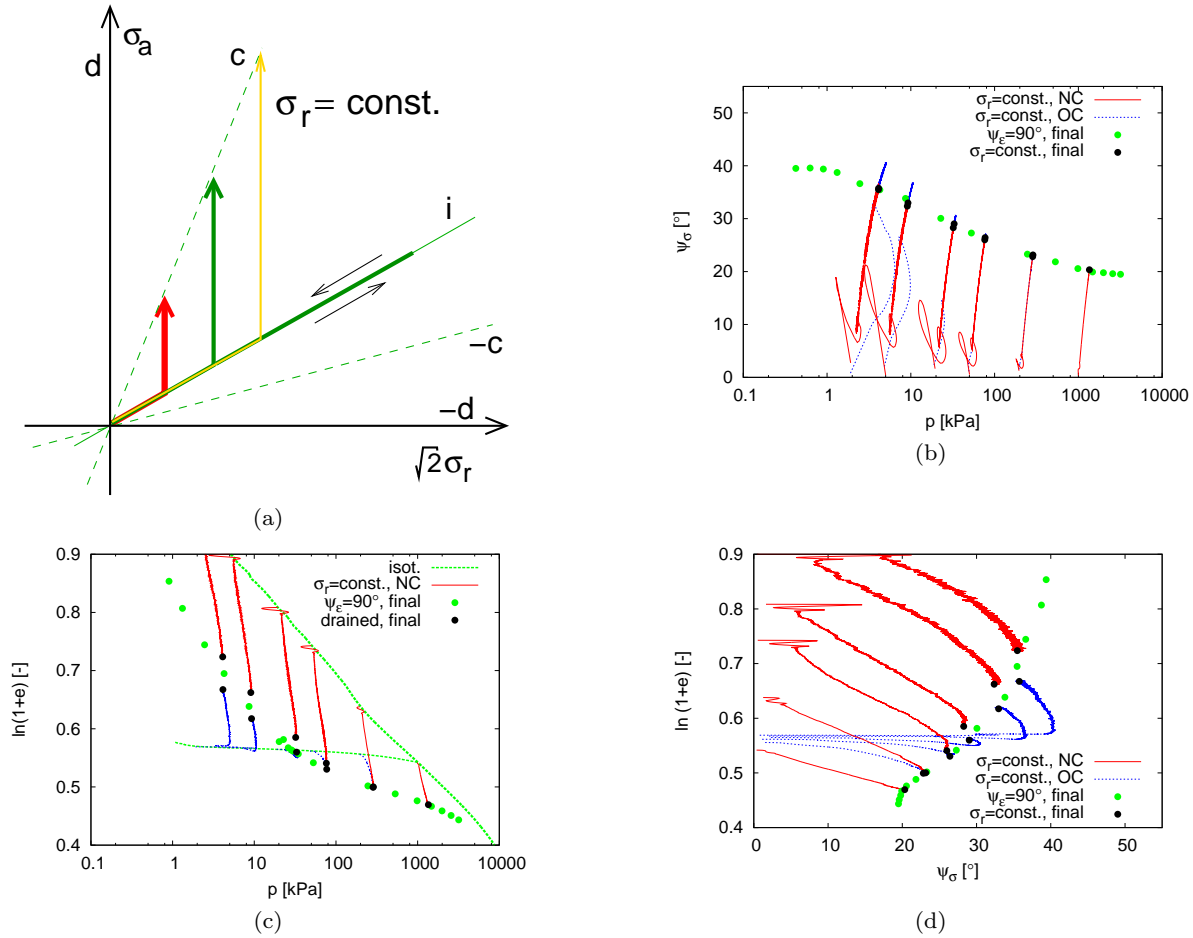


Fig. 13 Constant σ_r tests on normally consolidated and overconsolidated samples. (a) sketch of the stress paths expected from the theory, (b,c,d) results of DEM simulations. (b) ψ_σ vs. mean stress diagram, (c) normal compression lines in the $\ln(1+e)$ vs. $\log p$ plane, (d) ψ_σ vs. $\ln(1+e)$ diagram.

the isochoric stress path follows the state boundary surface up to the asymptotic state.

In drained triaxial tests (constant σ_r), the stress path direction is fixed, whereas the direction of ψ_ε varies. In Figure 19, stress and void ratio states with specific ψ_ε were extracted along constant σ_r test paths and compared with the asymptotic behaviour obtained in constant ψ_ε experiments. In general, reasonable agreement between the two data sets is obtained for the higher void ratios. In the lower void ratio range, more significant deviations occur, particularly in the range of lower ψ_σ values. The deviations may, however, be caused by non-negligible particle overlaps occurring at high stresses (Figure 8). Agreement between the two data sets would imply that at the ASBS the strain rate direction is independent of the stress rate direction. This assumption is implicit in elasto-plastic constitutive models. This was investigated using the DEM simulations by Tamagnini et al. [59], who did not confirm it.

It is particularly interesting to concentrate on the $\psi_\varepsilon = 95^\circ$ and $\psi_\varepsilon = 100^\circ$ state occurring near the peak of the constant σ_r test on heavily overconsolidated soil (unloaded from 1000 kPa to 2 kPa and 5 kPa), shown in Figure 19. This state plots close to the extension asymptotic state obtained by $\psi_\varepsilon = 95^\circ$ and $\psi_\varepsilon = 100^\circ$ stretching, respectively, thus supporting the structure of the critical state models, which consider that the peak states in drained triaxial test and extension asymptotic states coincide.

5 Discussion of the influence of the model characteristics

5.1 Inter-particle contact parameters

First, it has been verified that the actual contact parameter values do not qualitatively influence the results of the simulations. Special attention has been given to the influence of the coefficient of friction; Figure 20 shows

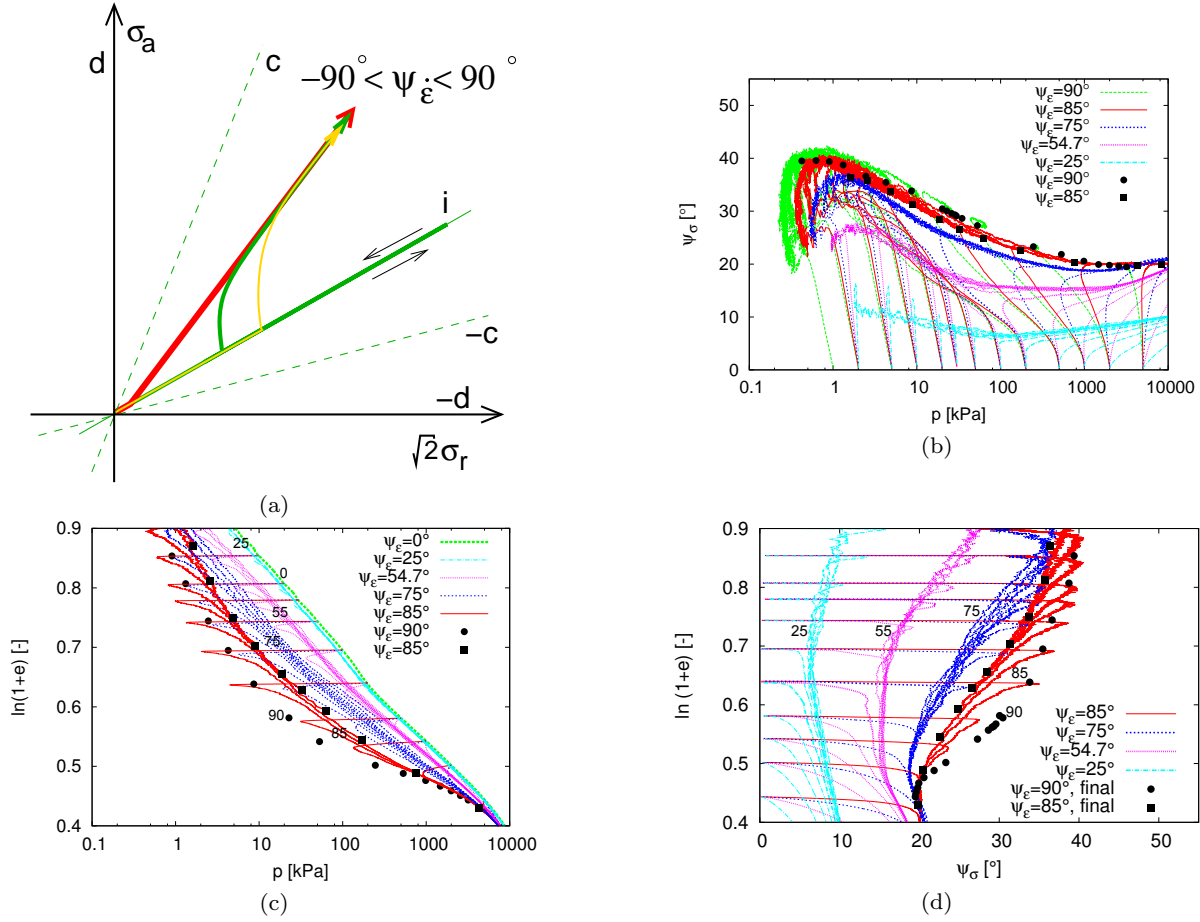


Fig. 14 Compression asymptotic states with $0^\circ \leq \psi_\varepsilon \leq 90^\circ$. (a) sketch of the stress paths expected from the theory, (b,c,d) results of DEM simulations. (b) ψ_σ vs. mean stress diagram, (c) normal compression lines in the $\ln(1+e)$ vs. $\log p$ plane, (d) ψ_σ vs. $\ln(1+e)$ diagram.

the response of the $\psi_\varepsilon = 0^\circ$ test (a) and $\psi_\varepsilon = 90^\circ$ test (b). Qualitatively similar results to those with frictional contact were obtained even for the case of $\varphi = 0$; the observed asymptotic behaviour can thus be attributed to both the structure of the granular material and to the inter-particle friction. Even a soil with $\varphi = 0$ has a certain frictional resistance, which further increases with an increase in the contact friction angle (Figure 20b).

5.2 Integration step size

One of the possible approaches to estimate critical time-step size ensuring stable numerical integration is based on the characteristic duration of contact (response time) t_c [49, 62, 35, 34, 14, 47]. For undamped oscillator, it reads

$$t_c = \frac{\pi}{\omega} \quad (3)$$

where $\omega = \sqrt{k_n/m_{12}}$ is the eigenfrequency of the contact, k_n is contact normal stiffness and $m_{12} = m_1 m_2 / (m_1 +$

$m_2)$ is the reduced mass of the two particles in contact. In the present case, t_c for the contact of smallest particles is $t_c(\min) = 1.5 \times 10^{-6}$ s, and t_c for the contact of largest particles is $t_c(\max) = 7.4 \times 10^{-6}$ s. The time-step size adopted in the present simulations was $\Delta t = 1.2 \times 10^{-7}$ s, which means $\Delta t = t_c(\min)/12.4 = t_c(\max)/61.9$. To verify the time-step size was sufficiently small, the simulations were repeated with five-times smaller Δt ; the results were identical.

5.3 Stretching rate

The results of discrete element simulations are in the dynamic regime influenced by the rate of shearing. Simulations of the simple plane shear tests by different authors [10, 26, 18, 50] revealed that the dependency of the global coefficient of friction μ^* on shear rate can be evaluated by means of a non-dimensional variable I ,

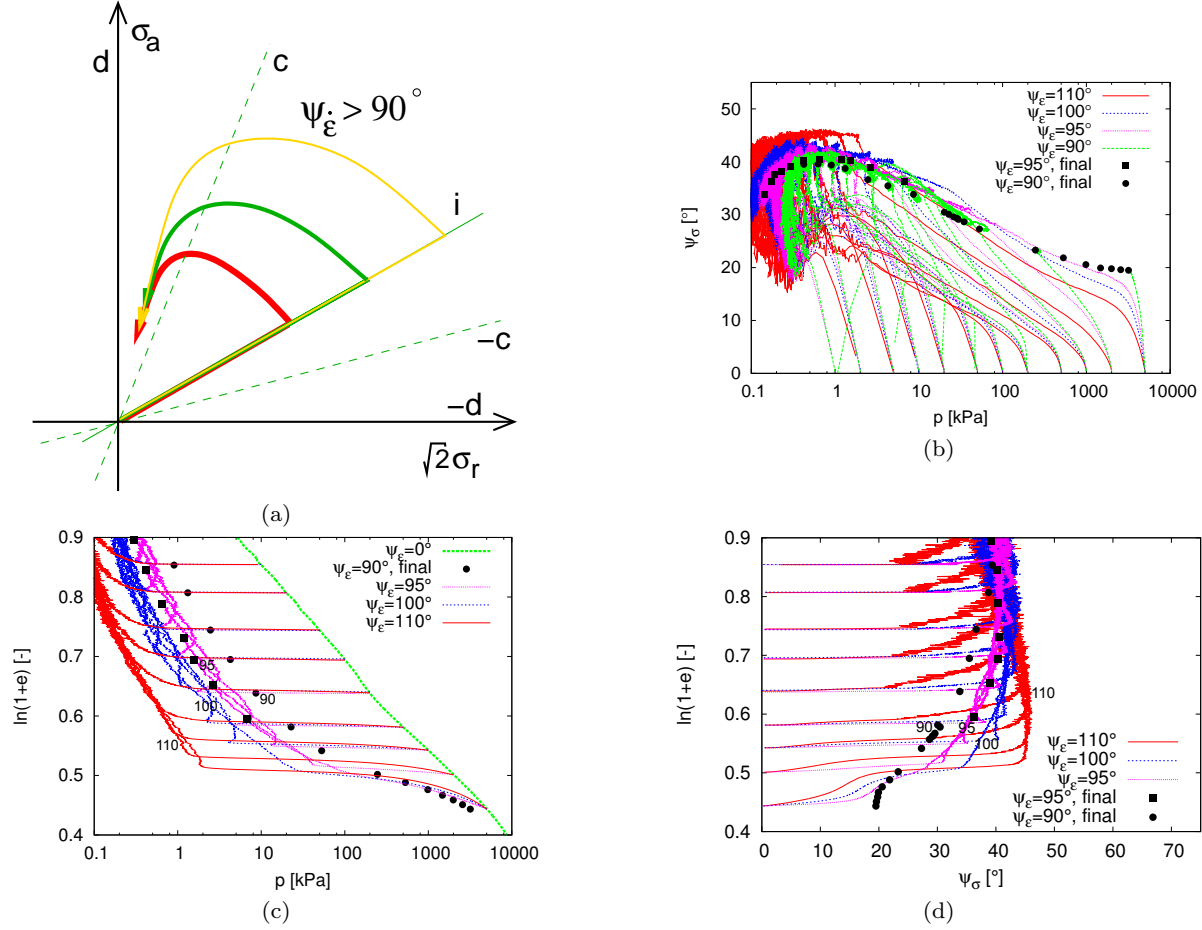


Fig. 15 Extension asymptotic states with $\psi_\epsilon \geq 90^\circ$. (a) sketch of the stress paths expected from the theory, (b,c,d) results of DEM simulations. (b) ψ_σ vs. mean stress diagram, (c) normal compression lines in the $\ln(1+e)$ vs. $\log p$ plane, (d) ψ_σ vs. $\ln(1+e)$ diagram.

called *inertial number* [10,18]. It is defined as

$$I = \frac{\dot{\gamma}d}{\sqrt{P/\rho_s}} \quad (4)$$

where $\dot{\gamma}$ is the shear rate, d is particle diameter and P is normal stress. For low values of the inertial number (approximately $I < 10^{-2}$), the simulations are quasi-static and the observed friction coefficient does not depend on the shear rate; for larger values of I , however, the global coefficient of friction μ^* increases with increasing I [10, 26,18,50]. This is demonstrated in Fig. 21 by Cruz et al. [10].

Generalisation of the inertial number for general loading has been proposed by Jop et al. [29]

$$I = \|\mathbf{D}\|d\sqrt{\frac{2\rho_s}{p}} \quad (5)$$

where p is mean stress. Figure 22 shows the values of I calculated for the smallest ($d = 0.2$ mm) and largest ($d = 1$ mm) particles within the system simulated in

this paper. Because the simulations are performed at a constant stretching rate $\|\mathbf{D}\|$, the inertial number depends on the stress level and increases with decreasing mean stress. In the lower stress range, the value of I is well above the limiting value $I = 10^{-2}$. The dependency of I on mean stress is likely the cause of the observed dependency of the asymptotic ψ_σ on mean stress level. Detailed investigation of this issue is outside the scope of the present paper and will be addressed in the future work.

6 Conclusions

In the paper, we investigated the existence of asymptotic states of granular assemblies and their characteristics. The concept was first introduced; asymptotic stress ratio, reached after sufficiently long stretching with a constant strain rate direction, is considered in soil mechanics to be a constant. We further introduced extension asymptotic states, and the notion of normal exten-

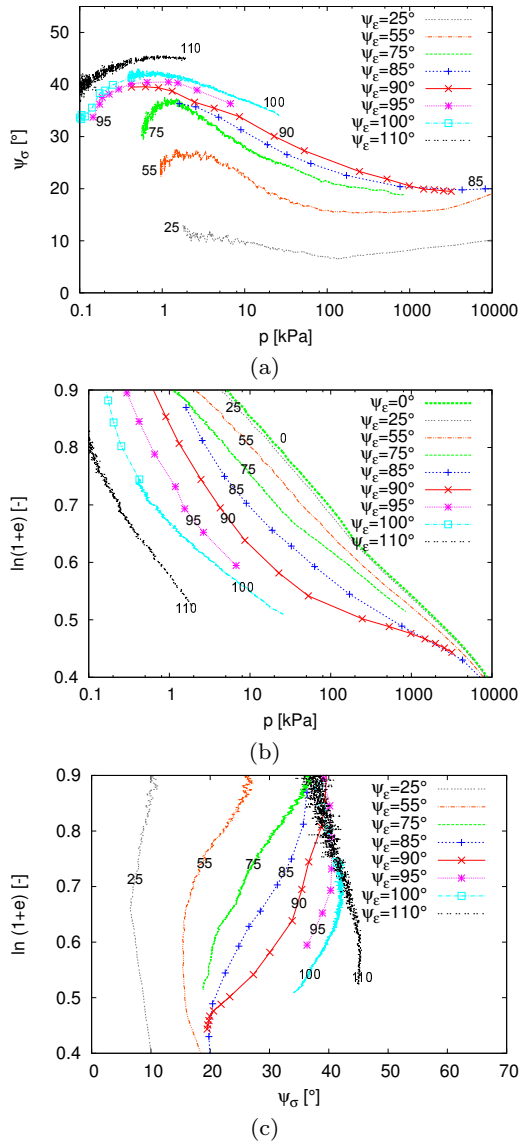


Fig. 16 Asymptotic states of an assembly of spherical particles, summary of the present DEM simulations. (a) ψ_σ vs. mean stress diagram, (b) normal compression lines in the $\ln(1+e)$ vs. $\log p$ plane, (c) ψ_σ vs. $\ln(1+e)$ diagram.

sion lines. It was pointed out that the asymptotic states are inherent in the critical state soil mechanics based constitutive models, although the existence of extension states has been investigated in detail in the past. We pointed out that many authors believe that the asymptotic behaviour is a consequence of grain crushing.

An extensive DEM study was undertaken. Although the particles were elastic (non-crushable), the asymptotic behaviour was clearly observed. Asymptotic behaviour thus appeared to be an inherent property of the granular assembly, caused primarily by particle rearrangement. The simulations indicated the existence of extension asymptotic states and normal extension lines.

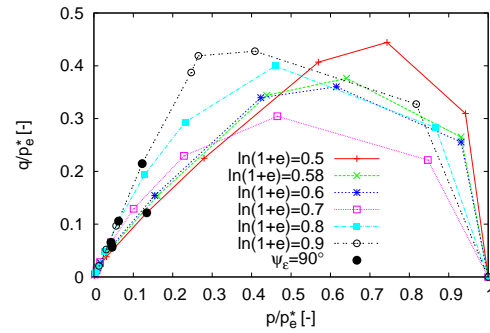


Fig. 17 Normalised constant volume cross-sections through ASBS for different void ratios. Plotted using data from Figure 16.

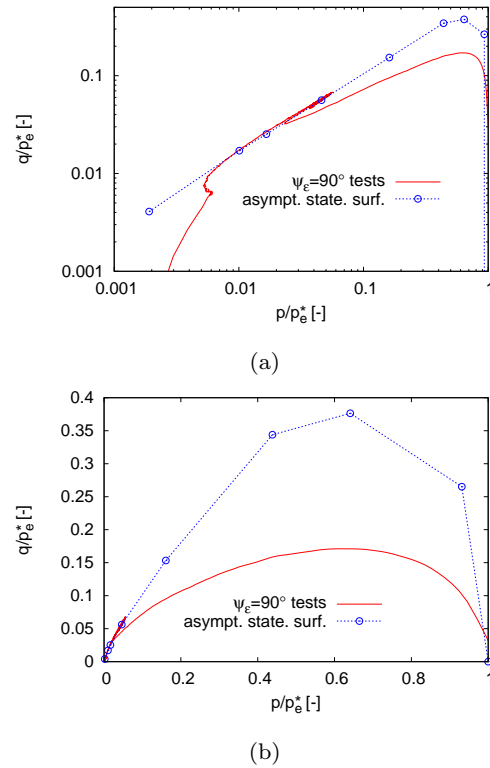


Fig. 18 Normalised cross-section through the ASBS at $\ln(1+e) = 0.58$ plotted together with $\psi_\epsilon = 90^\circ$ test results at the same void ratio and two overconsolidation ratios. (a) logarithmic scale, (b) linear scale.

We could not, however, investigate the behaviour up to limiting values of $\psi_\epsilon(\pm d)$; before reaching the asymptotic state, extremely low values of mean stresses were attained and then the results were scattered and unreliable. The asymptotic states were further compared with states along constant σ_r (drained) test paths. It was observed that the peak state in the drained test coincided with the extension asymptotic state. More generally, we could confirm the primary property of the critical state models, which assumes coincidence of the state

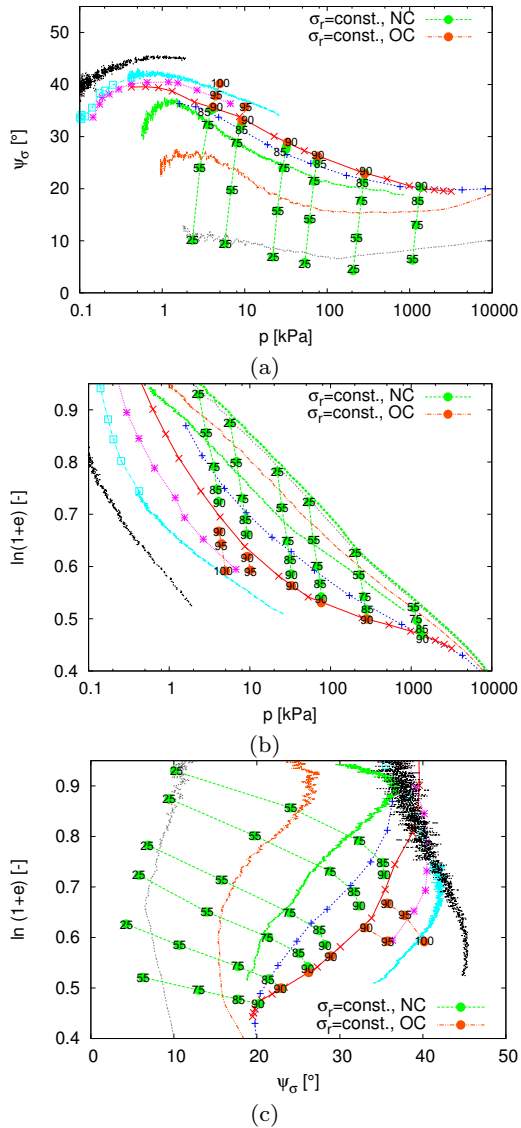


Fig. 19 Asymptotic state behaviour compared with strain rate directions in constant σ_r tests (labels for asymptotic states in Figure 16).

boundary and asymptotic state boundary surfaces. The asymptotic value of ψ_σ for the given ψ_ϵ was not constant, but depended on the mean stress. This fact was argued to be caused by the rate effects expressed in terms of the inertial number I .

Acknowledgements The author would like to thank to Prof. Gerd Gudehus for valuable discussions on the subject, to Dr. Václav Šmilauer for the introduction to the discrete element software Yade and to an anonymous journal reviewer for his valuable comments on the manuscript. Financial support by the research grants GACR P105/12/1705 and TACR TA01031840 is greatly appreciated.

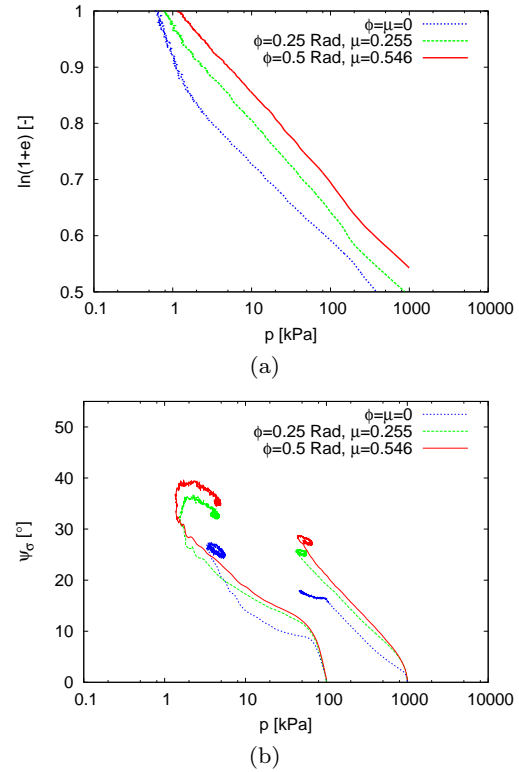


Fig. 20 The influence of the contact angle of friction ϕ (contact coefficient of friction μ) on the isotropic normal compression lines in the $\ln(1+e)$ vs. $\log p$ plane (a) and on the stress path of $\psi_\epsilon = 90^\circ$ tests under normally consolidated conditions.

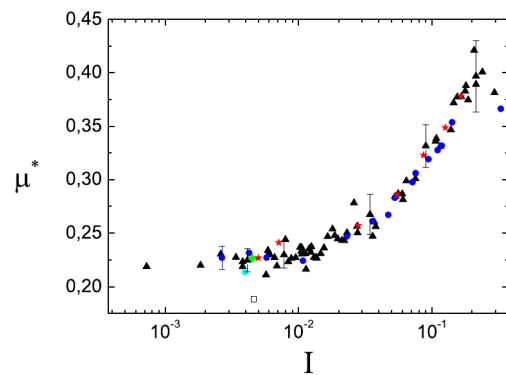


Fig. 21 Dependency of the global friction coefficient μ^* on the inertial number I for various values of restitution coefficients and inter-particle friction coefficients (data and figure from da Cruz et al. [10]).

References

1. Alonso-Marroquín, F., Luding, S., Herrmann, H.J., Vardoulakis, I.: Role of anisotropy in the elastoplastic response of a polygonal packing. *Phys. Rev. E* **71**, 051,304 (2005)
2. Ben-Nun, O., Einav, I., Tordesillas, A.: Force attractor in confined comminution of granular materials. *Physical Review Letters* **104**, 108,001–1/4 (2010)

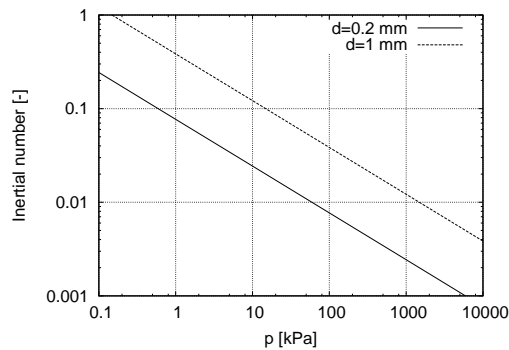


Fig. 22 The dependency of the inertial number I on mean stress p in the present simulations, calculated for the smallest and largest particles.

3. Butterfield, R.: A natural compression law for soils. *Géotechnique* **29**(4), 469–480 (1979)
4. Casagrande, A.: Characteristics of cohesionless soils affecting the stability of slopes and earth fills. *Journal of the Boston Society of Civil Engineers* **23**(Jan.), 257–276 (1936)
5. Chareyre, B., Villard, P.: Dynamic spar elements and discrete element methods in two dimensions for the modeling of soil-inclusion problems. *Journal of Engineering Mechanics* **131**(7), 689–698 (2005)
6. Chen, F., Drumm, E.C., Guiochon, G.: Prediction/verification of particle motion in one dimension with discrete element method. *Journal of Geotechnical and Geoenvironmental Engineering ASCE* **7**(5), 344–352 (2007)
7. Cheng, Y.P., Bolton, M.D., Nakata, Y.: Crushing and plastic deformation of soils simulated using DEM. *Géotechnique* **54**(2), 131–141 (2004)
8. Cheng, Y.P., Nakata, Y., Bolton, M.D.: Discrete element simulation of crushable soil. *Géotechnique* **53**(7), 633–641 (2003)
9. Chu, J., Lo, S.C.R.: Asymptotic behaviour of a granular soil in strain path testing. *Géotechnique* **44**(1), 65–82 (1994)
10. da Cruz, F., Emam, S., Prochnow, M., Roux, J.N., Chevoir, F.m.c.: Rheophysics of dense granular materials: Discrete simulation of plane shear flows. *Phys. Rev. E* **72**, 021,309 (2005)
11. Cundall, P.A.: Distinct element model of rock and soil structure. In: E.T. Brown (ed.) *Analytical and computational methods in engineering rock mechanics*, pp. 129–163. Allen & Unwin, London (1987)
12. Cundall, P.A., Hart, D.H.: Numerical modelling of discontinua. *Engineering Computations* **9**, 101–113 (1992)
13. Cundall, P.A., Strack, O.D.L.: A discrete numerical model for granular assemblies. *Géotechnique* **29**(1), 47–65 (1979)
14. David, C.T., García-Rojo, R., Herrmann, H.J., Luding, S.: Hysteresis and creep in powders and grains. In: H. García-Rojo, McNamara (eds.) *Powders and Grains*, pp. 291–294. Taylor and Francis, London (2005)
15. Donzé, F.V., Richefeu, V., Magnier, S.A.: Advances in discrete element method applied to soil, rock and concrete mechanics. In: *State of the art of geotechnical engineering*. *Electronic Journal of Geotechnical Engineering* p. 44 (2009)
16. Fedá, J.: Notes on the effect of grain crushing on the granular soil behaviour. *Engineering Geology* **63**, 93–98 (2002)
17. Ferrellec, J.F., McDowell, G.R.: A method to model realistic particle shape and inertia in DEM. *Granular Matter* **12**, 459–467 (2010)
18. GDR-MiDi: On dense granular flows. *The European Physical Journal E: Soft Matter and Biological Physics* **14**, 341–365 (2004)
19. Geng, J., Howell, D., Longhi, E., Behringer, R.P., Reydellet, G., Vanel, L., Clément, E., Luding, S.: Footprints in sand: The response of a granular material to local perturbations. *Phys. Rev. Lett.* **87**, 035,506 (2001)
20. Goldscheider, M.: True triaxial tests on dense sand. In: G. Gudehus (ed.) *Constitutive relations for soils*, pp. 11–54. Workshop Grenoble, Balkema (1982)
21. Gudehus, G.: Attractors for granular storage and flow. In: *3rd European Symposium – Storage and Flow of Particulate Solids*, Paper for the conf. 'Partec 95', pp. 333–345 (1995)
22. Gudehus, G.: Discussion of paper "Asymptotic behaviour of a granular soil in strain path testing" by Chu, J. and Lo, S.-C. R. *Géotechnique* **45**(2), 337–338 (1995)
23. Gudehus, G.: *Physical Soil Mechanics*. Springer, Berlin (2011)
24. Gudehus, G., Goldscheider, M., Winter, H.: Mechanical properties of sand and clay and numerical intergration methods: some sources of errors and bounds of accuracy. In: G. Gudehus (ed.) *Finite Elements in Geomechanics*, pp. 121–150. Wiley, Chichester (1977)
25. Gudehus, G., Mašín, D.: Graphical representation of constitutive equations. *Géotechnique* **59**(2), 147–151 (2009)
26. Hatano, T.: Constitutive law of dense granular matter. *Journal of Physics: Conference Series* **258**(1), 012,006 (2010)
27. Hvorslev, M.J.: Über die Festigkeitseigenschaften gestörter bindiger Böden. Ph.D. thesis, Danmarks naturvidenskabelige samfund, København (1937)
28. ITASCA: The PFC2D user's manual. ITASCA (2004). [Http://www.itascacg.com](http://www.itascacg.com)
29. Jop, P., Forterre, Y., Pouliquen, O.: A constitutive law for dense granular flows. *Nature* **441**, 727–730 (2006)
30. Kozicki, J., Teichman, J.: Numerical simulations of sand behaviour using DEM with two different descriptions of grain roughness. In: E. Oñate, D.R.J. Owen (eds.) *II International Conference on Particle-based Methods - Fundamentals and Applications. PARTICLES 2011* (2011)
31. Kuhl, E., DAddetta, G., Leukart, M., Ramm, E.: Microplane modelling and particle modelling of cohesive-frictional materials. In: P. Vermeer, H. Herrmann, S. Luding, W. Ehlers, S. Diebels, E. Ramm (eds.) *Continuous and Discontinuous Modelling of Cohesive-Frictional Materials, Lecture Notes in Physics*, vol. 568, pp. 31–46. Springer, Berlin / Heidelberg (2001)
32. Lätzel, M., Luding, S., Herrmann, H., Howell, D., Behringer, R.: Comparing simulation and experiment of a 2D granular couette shear device. *The European Physical Journal E: Soft Matter and Biological Physics* **11**, 325–333 (2003)
33. Lu, N., McDowell, G.R.: The importance of modelling ballast particle shape in the discrete element method. *Granular Matter* **9**, 69–80 (2007)
34. Luding, S.: Collisions & contacts between two particles. In: H.J. Herrmann, J.P. Hovi, S. Luding (eds.) *Physics of dry granular Media - NATO ASI Series E350*, p. 285. Kluwer Academic Publishers, Dordrecht (1998)
35. Luding, S.: Cohesive, frictional powders: contact models for tension. *Granular Matter* **10**(4), 235–246 (2008)

36. Luding, S., Alonso-Marroquín, F.: The critical state yield stress (termination locus) of adhesive powders from a single numerical experiment. *Granular Matter* **13**, 109–119 (2011)
37. Luo, T., Yao, Y., Chu, J.: Asymptotic state behaviour and its modeling for saturated sand. *Science in China Series E: Technological Sciences* **52**, 2350–2358 (2009)
38. Markauskas, D., Kašianauskas, R., Džiugys, A., Navakas, R.: Investigation of adequacy of multi-sphere approximation of elliptical particles for DEM simulations. *Granular Matter* **12**, 107–123 (2010)
39. Mašín, D.: A hypoplastic constitutive model for clays. *International Journal for Numerical and Analytical Methods in Geomechanics* **29**(4), 311–336 (2005)
40. Mašín, D.: Hypoplastic Cam-clay model. *Géotechnique* **62**(6), 549–553 (2012)
41. Mašín, D., Herle, I.: State boundary surface of a hypoplastic model for clays. *Computers and Geotechnics* **32**(6), 400–410 (2005)
42. Mašín, D., Herle, I.: Improvement of a hypoplastic model to predict clay behaviour under undrained conditions. *Acta Geotechnica* **2**(4), 261–268 (2007)
43. McDowell, G.R., Bolton, M.D.: On micromechanics of crushable aggregates. *Géotechnique* **48**(5), 667–679 (1998)
44. McDowell, G.R., Harireche, O.: Discrete element modelling of yielding and normal compression of sand. *Géotechnique* **52**(4), 299–304 (2002)
45. McDowell, G.R., Humphreys, A.: Yielding of granular materials. *Granular Matter* **4**, 1–8 (2002)
46. Miehe, C., Dettmar, J.: A framework for micromacro transitions in periodic particle aggregates of granular materials. *Comput. Methods Appl. Mech. Engrg.* **193**, 225–256 (2004)
47. Otsuki, M., Hayakawa, H., Luding, S.: Behavior of pressure and viscosity at high densities for two-dimensional hard and soft granular materials. *Progress of Theoretical Physics Supplement* **184**, 110–133 (2010)
48. Peña, A.A., Herrmann, H.J., Lizcano, A., Alonso-Marroquín, F.: Investigation of the asymptotic states of granular materials using discrete element model of anisotropic particles. In: H. García-Rojo, McNamara (eds.) *Powders and Grains*, pp. 697–700. Taylor and Francis, London (2005)
49. Peña, A.A., Lind, P.G., McNamara, S., Herrmann, H.J.: Geometrical derivation of frictional forces for granular media under slow shearing. *Acta Mechanica* **205**, 171–183 (2009)
50. Pouliquen, O., Cassar, C., Forterre, Y., Jop, P., Nicolas, M.: How do grains flow: towards a simple rheology for dense granular flows. In: H. García-Rojo, McNamara (eds.) *Powders and Grains*. Taylor and Francis, London (2005)
51. Radjai, F., Jean, M., Moreau, J.J., Roux, S.: Force distributions in dense two-dimensional granular systems. *Phys. Rev. Lett.* **77**, 274–277 (1996)
52. Roscoe, K.H., Burland, J.B.: On the generalised stress-strain behaviour of wet clay. In: J. Heyman, F.A. Leckie (eds.) *Engineering Plasticity*, pp. 535–609. Cambridge University Press, Cambridge (1968)
53. Salot, C., Gotteland, P., Villard, P.: Influence of relative density on granular materials behaviour: DEM simulations of triaxial tests. *Granular Matter* **11**, 221–236 (2009)
54. Schofield, A.N., Wroth, C.P.: *Critical State Soil Mechanics*. McGraw-Hill, London (1968)
55. Scholtés, L., Donzé, F.V., Khanal, M.: Scale effects on strength of geomaterials, case study: Coal. *Journal of the Mechanics and Physics of Solids* **59**, 1131–1146 (2011)
56. Sitharam, T.G., Vinod, J.S.: Critical state behaviour of granular materials from isotropic and rebounded paths: DEM simulations. *Granular Matter* **11**, 33–42 (2009)
57. Stahl, M., Konietzky, H.: Discrete element simulation of ballast and gravel under special consideration of grain-shape, grain-size and relative density. *Granular Matter* **13**(4), 417–428 (2011)
58. Stránský, J., Jirásek, M.: Calibration of particle-based models using cells with periodic boundary conditions. In: E. Oñate, D.R.J. Owen (eds.) *II International Conference on Particle-based Methods - Fundamentals and Applications. PARTICLES 2011* (2011)
59. Tamagnini, C., Calvetti, F., Viggiani, G.: An assesment of plasticity theories for modelling the incrementally non-linear behaviour of granular soils. *Journal of Engineering Mathematics* **52**, 265–291 (2005)
60. Taylor, D.W.: *Fundamentals of soil mechanics*. John Wiley, New York (1948)
61. Topolnicki, M., Gudehus, G., Mazurkiewicz, B.K.: Observed stress-strain behaviour of remoulded saturated clays under plane strain conditions. *Géotechnique* **40**(2), 155–187 (1990)
62. Tykhoniuk, R., Tomas, J., Luding, S., Kappl, M., Heim, L., Butt, H.J.: Ultrafine cohesive powders: From interparticle contacts to continuum behaviour. *Chemical Engineering Science* **62**(11), 28432864 (2007)
63. Smilauer, V., Catalano, E., Chareyre, B., Dorofenko, S., Duriez, J., Gladky, A., Kozicki, J., Modenese, C., Scholtés, L., Sibille, L., Stránský, J., Thoeni, K.: *Yade Documentation*, 1st edn. The Yade Project (2010). [Http://yade-dem.org/doc/](http://yade-dem.org/doc/)
64. Walker, D.M., Tordesillas, A., Einav, I., Small, M.: Complex networks in confined comminution. *Physical Review E* **84**, 021,301–1/9 (2011)
65. Wang, J., Yu, H.S., Langston, P., Fraige, F.: Particle shape effects in discrete element modelling of cohesive angular particles. *Granular Matter* **13**, 1–12 (2011)
66. von Wolffersdorff, P.A.: A hypoplastic relation for granular materials with a predefined limit state surface. *Mechanics of Cohesive-Frictional Materials* **1**, 251–271 (1996)
67. Zhao, X., Evans, T.M.: Numerical analysis of critical state behaviors of granular soils under different loading conditions. *Granular Matter* **13**, 751–764 (2011)